Inclusive Σ^- and $\Lambda(1520)$ production in hadronic Z decays

DELPHI Collaboration

Abstract

Production of Σ^- and $\Lambda(1520)$ in hadronic Z decays has been measured using the DELPHI detector at LEP. The Σ^- is directly reconstructed as a charged track in the DELPHI microvertex detector and is identified by its $\Sigma \to n\pi$ decay leading to a kink between the Σ^- and π-track. The reconstruction of the $\Lambda(1520)$ resonance relies strongly on the particle identification capabilities of the barrel Ring Imaging Cherenkov detector and on the ionisation loss measurement of the TPC. Inclusive production spectra are measured for both particles. The production rates are measured to be

$$
\begin{aligned}
\langle N_{\Sigma^-}/N_Z^{\mathrm{had}}\rangle &= 0.081 \pm 0.002 \pm 0.010 \;, \\
\langle N_{\Lambda(1520)}/N_Z^{\mathrm{had}}\rangle &= 0.029 \pm 0.005 \pm 0.005 \;.
\end{aligned}
$$

The production rate of the $\Lambda(1520)$ suggests that a large fraction of the stable baryons descend from orbitally excited baryonic states. It is shown that the baryon production rates in Z decays follow a universal phenomenological law related to isospin, strangeness and mass of the particles.

P.Abreu[22], W.Adam[52], T.Adye[38], P.Adzic[12], I.Ajinenko[44], Z.Albrecht[18], T.Alderweireld[2], G.D.Alekseev[17], R.Alemany[51], T.Allmendinger[18], P.P.Allport[23], S.Almehed[25], U.Amaldi[9,29], N.Amapane[47], S.Amato[49], E.G.Anassontzis[3], P.Andersson[46], A.Andreazza[9], S.Andringa[22], P.Antilogus[26], W-D.Apel[18], Y.Arnoud[9], B.Åsman[46], J-E.Augustin[26], A.Augustinus[9], P.Baillon[9], A.Ballestrero[47], P.Bambade[20], F.Barao[22], G.Barbiellini[48], R.Barbier[26], D.Y.Bardin[17], G.Barker[18], A.Baroncelli[40], M.Battaglia[16], M.Baubillier[24], K-H.Becks[54], M.Begalli[6], A.Behrmann[54], P.Beilliere[8], Yu.Belokopytov[9], N.C.Benekos[33], A.C.Benvenuti[5], C.Berat[15], M.Berggren[24], D.Bertrand[2], M.Besancon[41], M.Bigi[47], M.S.Bilenky[17], M-A.Bizouard[20], D.Bloch[10], H.M.Blom[32], M.Bonesini[29], M.Boonekamp[41], P.S.L.Booth[23], G.Borisov[20], C.Bosio[43], O.Botner[50], E.Boudinov[32], B.Bouquet[20], C.Bourdarios[20], T.J.V.Bowcock[23], I.Boyko[17], I.Bozovic[12], M.Bozzo[14], M.Bracko[45], P.Branchini[40], R.A.Brenner[50], P.Bruckman[9], J-M.Brunet[8], L.Bugge[34], T.Buran[34], B.Buschbeck[52], P.Buschmann[54], S.Cabrera[51], M.Caccia[28], M.Calvi[29], T.Camporesi[9], V.Canale[39], F.Carena[9], L.Carroll[23], C.Caso[14], M.V.Castillo Gimenez[51], A.Cattai[9], F.R.Cavallo[5], V.Chabaud[9], Ph.Charpentier[9], P.Checchia[37], G.A.Chelkov[17], R.Chierici[47], P.Chliapnikov[9,44], P.Chochula[7], V.Chorowicz[26], J.Chudoba[31], K.Cieslik[19], P.Collins[9], R.Contri[14], E.Cortina[51], G.Cosme[20], F.Cossutti[9], M.Costa[51], H.B.Crawley[1], D.Crennell[38], S.Crepe[15], G.Crosetti[14], J.Cuevas Maestro[35], S.Czellar[16], M.Davenport[9], W.Da Silva[24], G.Della Ricca[48], P.Delpierre[27], N.Demaria[9], A.De Angelis[48], W.De Boer[18], C.De Clercq[2], B.De Lotto[48], A.De Min[37], L.De Paula[49], H.Dijkstra[9], L.Di Ciaccio[9,39], J.Dolbeau[8], K.Doroba[53], M.Dracos[10], J.Drees[54], M.Dris[33], A.Duperrin[26], J-D.Durand[9], G.Eigen[4], T.Ekelof[50], G.Ekspong[46], M.Ellert[50], M.Elsing[9], J-P.Engel[10], M.Espirito Santo[9], G.Fanourakis[12], D.Fassouliotis[12], J.Fayot[24], M.Feindt[18], A.Ferrer[51], E.Ferrer-Ribas[20], F.Ferro[14], S.Fichet[24], A.Firestone[1], U.Flagmeyer[54], H.Foeth[9], E.Fokitis[33], F.Fontanelli[14], B.Franek[38], A.G.Frodesen[4], R.Fruhwirth[52], F.Fulda-Quenzer[20], J.Fuster[51], A.Galloni[23], D.Gamba[47], S.Gamblin[20], M.Gandelman[49], C.Garcia[51], C.Gaspar[9], M.Gaspar[49], U.Gasparini[37], Ph.Gavillet[9], E.N.Gazis[33], D.Gele[10], T.Geralis[12], L.Gerdyukov[44], N.Ghodbane[26], I.Gil[51], F.Glege[54], R.Gokieli[9,53], B.Golob[9,45], G.Gomez-Ceballos[42], P.Goncalves[22], I.Gonzalez Caballero[42], G.Gopal[38], L.Gorn[1], Yu.Gouz[44], V.Gracco[14], J.Grahl[1], E.Graziani[40], P.Gris[41], G.Grosdidier[20], K.Grzelak[53], J.Guy[38], C.Haag[18], F.Hahn[9], S.Hahn[54], S.Haider[9], A.Hallgren[50], K.Hamacher[54], J.Hansen[34], F.J.Harris[36], F.Hauler[18], V.Hedberg[9,25], S.Heising[18], J.J.Hernandez[51], P.Herquet[2], H.Herr[9], T.L.Hessing[36], J.-M.Heuser[54], E.Higon[51], S-O.Holmgren[46], P.J.Holt[36], S.Hoorelbeke[2], M.Houlden[23], J.Hrubec[52], M.Huber[18], K.Huet[2], G.J.Hughes[23], K.Hultqvist[9,46], J.N.Jackson[23], R.Jacobsson[9], P.Jalocha[19], R.Janik[7], Ch.Jarlskog[25], G.Jarlskog[25], P.Jarry[41], B.Jean-Marie[20], D.Jeans[36], E.K.Johansson[46], P.Jonsson[26], C.Joram[9], P.Juillot[10], L.Jungermann[18], F.Kapusta[24], K.Karafasoulis[12], S.Katsanevas[26], E.C.Katsoufis[33], R.Keranen[18], G.Kernel[45], B.P.Kersevan[45], Yu.Khokhlov[44], B.A.Khomenko[17], N.N.Khovanski[17], A.Kiiskinen[16], B.King[23], A.Kinvig[23], N.J.Kjaer[9], O.Klapp[54], H.Klein[9], P.Kluit[32], P.Kokkinias[12], V.Kostioukhine[44], C.Kourkoumelis[3], O.Kouznetsov[17], M.Krammer[52], E.Kriznic[45], Z.Krumstein[17], P.Kubinec[7], J.Kurowska[53], K.Kurvinen[16], J.W.Lamsa[1], D.W.Lane[1], J-P.Laugier[41], R.Lauhakangas[16], G.Leder[52], F.Ledroit[15], V.Lefebure[2], L.Leinonen[46], A.Leisos[12], R.Leitner[31], G.Lenzen[54], V.Lepeltier[20], T.Lesiak[19], M.Lethuillier[41], J.Libby[36], W.Liebig[54], D.Liko[9], A.Lipniacka[9,46], I.Lippi[37], B.Loerstad[25], J.G.Loken[36], J.H.Lopes[49], J.M.Lopez[42], R.Lopez-Fernandez[15], D.Loukas[12], P.Lutz[41], L.Lyons[36], J.MacNaughton[52], J.R.Mahon[6], A.Maio[22], A.Malek[54], T.G.M.Malmgren[46], S.Maltezos[33], V.Malychev[17], F.Mandl[52], J.Marco[42], R.Marco[42], B.Marechal[49], M.Margoni[37], J-C.Marin[9], C.Mariotti[9], A.Markou[12], C.Martinez-Rivero[20], S.Marti i Garcia[9], J.Masik[13], N.Mastroyiannopoulos[12], F.Matorras[42], C.Matteuzzi[29], G.Matthiae[39], F.Mazzucato[37], M.Mazzucato[37], M.Mc Cubbin[23], R.Mc Kay[1], R.Mc Nulty[23], G.Mc Pherson[23], C.Meroni[28], W.T.Meyer[1], E.Migliore[9], L.Mirabito[26], W.A.Mitaroff[52], U.Mjoernmark[25], T.Moa[46], M.Moch[18], R.Moeller[30], K.Moenig[9,11], M.R.Monge[14], D.Moraes[49], X.Moreau[24], P.Morettini[14], G.Morton[36], U.Mueller[54], K.Muenich[54], M.Mulders[32], C.Mulet-Marquis[15], R.Muresan[25], W.J.Murray[38], B.Muryn[19], G.Myatt[36], T.Myklebust[34], F.Naraghi[15], M.Nassiakou[12], F.L.Navarria[5], K.Nawrocki[53], P.Negri[29], N.Neufeld[9], R.Nicolaidou[41], B.S.Nielsen[30], P.Niezurawski[53], M.Nikolenko[10,17], V.Nomokonov[16], A.Nygren[25], V.Obraztsov[44], A.G.Olshevski[17], A.Onofre[22], R.Orava[16], G.Orazi[10], K.Osterberg[16], A.Ouraou[41], A.Oyanguren[51], M.Paganoni[29], S.Paiano[5], R.Pain[24], R.Paiva[22], J.Palacios[36], H.Palka[19], Th.D.Papadopoulou[9,33], L.Pape[9], C.Parkes[9], F.Parodi[14], U.Parzefall[23], A.Passeri[40], O.Passon[54], T.Pavel[25], M.Pegoraro[37], L.Peralta[22], M.Pernicka[52], A.Perrotta[5], C.Petridou[48], A.Petrolini[14], H.T.Phillips[38], F.Pierre[41], M.Pimenta[22], E.Piotto[28], T.Podobnik[45], M.E.Pol[6], G.Polok[19], P.Poropat[48], V.Pozdniakov[17], P.Privitera[39], N.Pukhaeva[17], A.Pullia[29], D.Radojicic[36], S.Ragazzi[29], H.Rahmani[33], J.Rames[13], P.N.Ratoff[21], A.L.Read[34], P.Rebecchi[9], N.G.Redaelli[29], M.Regler[52], J.Rehn[18], D.Reid[32], P.Reinertsen[4], R.Reinhardt[54], P.B.Renton[36], L.K.Resvanis[3], F.Richard[20], J.Ridky[13], G.Rinaudo[47], I.Ripp-Baudot[10], O.Rohne[34], A.Romero[47], P.Ronchese[37], E.I.Rosenberg[1], P.Rosinsky[7], P.Roudeau[20], T.Rovelli[5], Ch.Royon[41], V.Ruhlmann-Kleider[41], A.Ruiz[42], H.Saarikko[16], Y.Sacquin[41], A.Sadovsky[17], G.Sajot[15], J.Salt[51], D.Sampsonidis[12], M.Sannino[14], Ph.Schwemling[24], B.Schwering[54], U.Schwickerath[18], F.Scuri[48], P.Seager[21], Y.Sedykh[17], F.Seemann[54], A.M.Segar[36], N.Seibert[18], R.Sekulin[38], R.C.Shellard[6], M.Siebel[54], L.Simard[41], F.Simonetto[37], A.N.Sisakian[17], G.Smadja[26], N.Smirnov[44], O.Smirnova[25], G.R.Smith[38], A.Sokolov[44], O.Solovianov[44], A.Sopczak[18], R.Sosnowski[53], T.Spassov[22], E.Spiriti[40], S.Squarcia[14], C.Stanescu[40], S.Stanic[45], M.Stanitzki[18], K.Stevenson[36], A.Stocchi[20], J.Strauss[52], R.Strub[10], B.Stugu[4], M.Szczekowski[53], M.Szeptycka[53], T.Tabarelli[29], A.Taffard[23], F.Tegenfeldt[50], F.Terranova[29], J.Thomas[36], J.Timmermans[32], N.Tinti[5], L.G.Tkatchev[17], M.Tobin[23], S.Todorova[9], A.Tomaradze[2], B.Tome[22], A.Tonazzo[9], L.Tortora[40], P.Tortosa[51], G.Transtromer[25], D.Treille[9], G.Tristram[8], M.Trochimczuk[53], C.Troncon[28], M-L.Turluer[41],

I.A.Tyapkin[17], P.Tyapkin[25], S.Tzamarias[12], O.Ullaland[9], V.Uvarov[44], G.Valenti[9,5], E.Vallazza[48], P.Van Dam[32], W.Van den Boeck[2], J.Van Eldik[9,32], A.Van Lysebetten[2], N.van Remortel[2], I.Van Vulpen[32], G.Vegni[28], L.Ventura[37], W.Venus[38,9], F.Verbeure[2], P.Verdier[26], M.Verlato[37], L.S.Vertogradov[17], V.Verzi[28], D.Vilanova[41], L.Vitale[48], E.Vlasov[44], A.S.Vodopyanov[17], G.Voulgaris[3], V.Vrba[13], H.Wahlen[54], C.Walck[46], A.J.Washbrook[23], C.Weiser[9], D.Wicke[9], J.H.Wickens[2], G.R.Wilkinson[36], M.Winter[10], M.Witek[19], G.Wolf[9], J.Yi[1], O.Yushchenko[44], A.Zalewska[19], P.Zalewski[53], D.Zavrtanik[45], E.Zevgolatakos[12], N.I.Zimin[17,25], A.Zintchenko[17], Ph.Zoller[10], G.C.Zucchelli[46], G.Zumerle[37], W.Oberschulte gen. Beckmann[18]

[1]Department of Physics and Astronomy, Iowa State University, Ames IA 50011-3160, USA
[2]Physics Department, Univ. Instelling Antwerpen, Universiteitsplein 1, B-2610 Antwerpen, Belgium
 and IIHE, ULB-VUB, Pleinlaan 2, B-1050 Brussels, Belgium
 and Faculté des Sciences, Univ. de l'Etat Mons, Av. Maistriau 19, B-7000 Mons, Belgium
[3]Physics Laboratory, University of Athens, Solonos Str. 104, GR-10680 Athens, Greece
[4]Department of Physics, University of Bergen, Allégaten 55, NO-5007 Bergen, Norway
[5]Dipartimento di Fisica, Università di Bologna and INFN, Via Irnerio 46, IT-40126 Bologna, Italy
[6]Centro Brasileiro de Pesquisas Físicas, rua Xavier Sigaud 150, BR-22290 Rio de Janeiro, Brazil
 and Depto. de Física, Pont. Univ. Católica, C.P. 38071 BR-22453 Rio de Janeiro, Brazil
 and Inst. de Física, Univ. Estadual do Rio de Janeiro, rua São Francisco Xavier 524, Rio de Janeiro, Brazil
[7]Comenius University, Faculty of Mathematics and Physics, Mlynska Dolina, SK-84215 Bratislava, Slovakia
[8]Collège de France, Lab. de Physique Corpusculaire, IN2P3-CNRS, FR-75231 Paris Cedex 05, France
[9]CERN, CH-1211 Geneva 23, Switzerland
[10]Institut de Recherches Subatomiques, IN2P3 - CNRS/ULP - BP20, FR-67037 Strasbourg Cedex, France
[11]Now at DESY-Zeuthen, Platanenallee 6, D-15735 Zeuthen, Germany
[12]Institute of Nuclear Physics, N.C.S.R. Demokritos, P.O. Box 60228, GR-15310 Athens, Greece
[13]FZU, Inst. of Phys. of the C.A.S. High Energy Physics Division, Na Slovance 2, CZ-180 40, Praha 8, Czech Republic
[14]Dipartimento di Fisica, Università di Genova and INFN, Via Dodecaneso 33, IT-16146 Genova, Italy
[15]Institut des Sciences Nucléaires, IN2P3-CNRS, Université de Grenoble 1, FR-38026 Grenoble Cedex, France
[16]Helsinki Institute of Physics, HIP, P.O. Box 9, FI-00014 Helsinki, Finland
[17]Joint Institute for Nuclear Research, Dubna, Head Post Office, P.O. Box 79, RU-101 000 Moscow, Russian Federation
[18]Institut für Experimentelle Kernphysik, Universität Karlsruhe, Postfach 6980, DE-76128 Karlsruhe, Germany
[19]Institute of Nuclear Physics and University of Mining and Metalurgy, Ul. Kawiory 26a, PL-30055 Krakow, Poland
[20]Université de Paris-Sud, Lab. de l'Accélérateur Linéaire, IN2P3-CNRS, Bât. 200, FR-91405 Orsay Cedex, France
[21]School of Physics and Chemistry, University of Lancaster, Lancaster LA1 4YB, UK
[22]LIP, IST, FCUL - Av. Elias Garcia, 14-1°, PT-1000 Lisboa Codex, Portugal
[23]Department of Physics, University of Liverpool, P.O. Box 147, Liverpool L69 3BX, UK
[24]LPNHE, IN2P3-CNRS, Univ. Paris VI et VII, Tour 33 (RdC), 4 place Jussieu, FR-75252 Paris Cedex 05, France
[25]Department of Physics, University of Lund, Sölvegatan 14, SE-223 63 Lund, Sweden
[26]Université Claude Bernard de Lyon, IPNL, IN2P3-CNRS, FR-69622 Villeurbanne Cedex, France
[27]Univ. d'Aix - Marseille II - CPP, IN2P3-CNRS, FR-13288 Marseille Cedex 09, France
[28]Dipartimento di Fisica, Università di Milano and INFN-MILANO, Via Celoria 16, IT-20133 Milan, Italy
[29]Dipartimento di Fisica, Univ. di Milano-Bicocca and INFN-MILANO, Piazza delle Scienze 2, IT-20126 Milan, Italy
[30]Niels Bohr Institute, Blegdamsvej 17, DK-2100 Copenhagen Ø, Denmark
[31]IPNP of MFF, Charles Univ., Areal MFF, V Holesovickach 2, CZ-180 00, Praha 8, Czech Republic
[32]NIKHEF, Postbus 41882, NL-1009 DB Amsterdam, The Netherlands
[33]National Technical University, Physics Department, Zografou Campus, GR-15773 Athens, Greece
[34]Physics Department, University of Oslo, Blindern, NO-1000 Oslo 3, Norway
[35]Dpto. Fisica, Univ. Oviedo, Avda. Calvo Sotelo s/n, ES-33007 Oviedo, Spain
[36]Department of Physics, University of Oxford, Keble Road, Oxford OX1 3RH, UK
[37]Dipartimento di Fisica, Università di Padova and INFN, Via Marzolo 8, IT-35131 Padua, Italy
[38]Rutherford Appleton Laboratory, Chilton, Didcot OX11 OQX, UK
[39]Dipartimento di Fisica, Università di Roma II and INFN, Tor Vergata, IT-00173 Rome, Italy
[40]Dipartimento di Fisica, Università di Roma III and INFN, Via della Vasca Navale 84, IT-00146 Rome, Italy
[41]DAPNIA/Service de Physique des Particules, CEA-Saclay, FR-91191 Gif-sur-Yvette Cedex, France
[42]Instituto de Fisica de Cantabria (CSIC-UC), Avda. los Castros s/n, ES-39006 Santander, Spain
[43]Dipartimento di Fisica, Università degli Studi di Roma La Sapienza, Piazzale Aldo Moro 2, IT-00185 Rome, Italy
[44]Inst. for High Energy Physics, Serpukov P.O. Box 35, Protvino, (Moscow Region), Russian Federation
[45]J. Stefan Institute, Jamova 39, SI-1000 Ljubljana, Slovenia and Laboratory for Astroparticle Physics,
 Nova Gorica Polytechnic, Kostanjeviska 16a, SI-5000 Nova Gorica, Slovenia,
 and Department of Physics, University of Ljubljana, SI-1000 Ljubljana, Slovenia
[46]Fysikum, Stockholm University, Box 6730, SE-113 85 Stockholm, Sweden
[47]Dipartimento di Fisica Sperimentale, Università di Torino and INFN, Via P. Giuria 1, IT-10125 Turin, Italy
[48]Dipartimento di Fisica, Università di Trieste and INFN, Via A. Valerio 2, IT-34127 Trieste, Italy
 and Istituto di Fisica, Università di Udine, IT-33100 Udine, Italy
[49]Univ. Federal do Rio de Janeiro, C.P. 68528 Cidade Univ., Ilha do Fundão BR-21945-970 Rio de Janeiro, Brazil
[50]Department of Radiation Sciences, University of Uppsala, P.O. Box 535, SE-751 21 Uppsala, Sweden
[51]IFIC, Valencia-CSIC, and D.F.A.M.N., U. de Valencia, Avda. Dr. Moliner 50, ES-46100 Burjassot (Valencia), Spain
[52]Institut für Hochenergiephysik, Österr. Akad. d. Wissensch., Nikolsdorfergasse 18, AT-1050 Vienna, Austria
[53]Inst. Nuclear Studies and University of Warsaw, Ul. Hoza 69, PL-00681 Warsaw, Poland
[54]Fachbereich Physik, University of Wuppertal, Postfach 100 127, DE-42097 Wuppertal, Germany

1 Introduction

The study of baryon production provides an important tool to test models of the fragmentation process [1]. Beyond the cluster fragmentation model [2], and the string model [3] which employs many parameters to describe baryon fragmentation, thermodynamical [4] and phenomenological models [5,6,7] have appeared recently which successfully describe the overall particle production rates in high energy interactions with very few parameters.

At LEP it has been shown that a large fraction of the observed stable mesons stem from decays of scalar and tensor mesons with angular momentum. For baryons this is not the case, as baryon resonances, especially those with orbital excitations, typically have a large decay width and complicated decay modes. Hence these states are difficult to access experimentally in a multihadronic environment. In any case, it is still a question of basic importance as to how far baryon production leads to excited baryonic states.

So far the only orbitally excited baryonic state measured in e^+e^- annihilation is the $\Lambda(1520)$ [8,9]. This paper provides further data on $\Lambda(1520)$ and Σ^- production[1] in hadronic Z decays. For Σ^- production at the Z so far only two measurements are available [10,11], one of them being sensitive only to the sum of Σ^- and Σ^+ states [10].

The data used throughout this paper were collected by the DELPHI detector in 1994 and 1995. In these data taking periods the DELPHI microVertex (VD) and Ring Imaging Cherenkov (RICH) detectors were optimally set up and functioning for the analyses presented.

This paper is organised as follows. Section (2) gives a brief overview on the detector, experimental procedures used to select tracks and hadronic events as well as on the specific experimental procedures and corrections used for Σ^- and $\Lambda(1520)$ reconstruction. Section (3) presents the results for Σ^- and $\Lambda(1520)$ production and the corresponding systematic errors. These results are compared to the expectation of fragmentation models and a general phenomenological law of baryon production in Z decays is deduced. Finally we conclude in Section (4).

2 The Experimental Procedure and Event Selection

The DELPHI detector is described in detail in [12]. The present analysis relies on information provided by the central tracking detectors and the barrel RICH:

- The **microVertex Detector** (VD) consists of three layers of silicon strip detectors at radii of 6.3, 9.0 and 10.9 cm. $R\phi$ coordinates[2] in the plane perpendicular to the beam are measured in all three layers. The first and third layers also provide z information. The polar angle (θ) coverage for a particle passing all three layers is from 44° to 136°. The single point resolution has been estimated from real data to be about 8 μm in $R\phi$ and (for charged particles crossing perpendicular to the module) about 9 μm in z.
- The **Inner Detector** (ID) consists of an inner drift chamber with jet chamber geometry and 5 cylindrical MWPC (in 1995 straw tube) layers. The jet chamber,

---

[1]The antiparticles are always implicitly included.

[2]In the standard DELPHI coordinate system, the z axis is along the electron direction, the x axis points towards the centre of LEP, and the y axis points upwards. The polar angle to the z axis is denoted by θ, and the azimuthal angle around the z axis by ϕ; the radial coordinate is $R = \sqrt{x^2 + y^2}$.

between 12 and 23 cm in R and 23° and 157° (15°-165° for 1995) in θ, consists of 24 azimuthal sectors, each providing up to 24 $R\phi$ points.

- The **Time Projection Chamber** (TPC) is the main tracking device of DELPHI. It provides up to 16 space points per particle trajectory for radii between 40 and 110 cm. The precision on the track elements is about 150 μm in $R\phi$ and about 600 μm in z. A measurement of the energy loss dE/dx of a track is provided with a resolution of about 6.5%.
- The **Outer Detector** (OD) is a 4.7 m long set of 5 layers of drift tubes situated at 2 m radius to the beam which provides precise spatial information in $R\phi$.
- The **Barrel Ring Imaging Cherenkov Counter** (BRICH) is the main DELPHI detector devoted to charged particle identification. It is subdivided into two halves ($z \gtrless 0$) and provides particle identification using Cherenkov radiation produced in a liquid or a gas radiator. This radiation, after appropriate focusing, is transformed into photoelectrons in a TPC-like drift structure and the Cherenkov angles of the track in both media are determined. The BRICH detector provides particle identification in the momentum range 0.7 to 45 GeV/c.

An event was selected as a multihadronic event if the following requirements were satisfied:

- There were at least five well measured charged particles in the event, each with momentum larger than 300 MeV/c (400 MeV/c for the Σ^- analysis) and a polar angle in the range $20° < \theta < 160°$.
- The total reconstructed energy of these charged tracks had to be larger than 12% of the centre-of-mass energy.
- The total energy of the charged particles in each detector hemisphere (defined by the plane perpendicular to the beam axis) had to exceed 3% of the centre-of-mass energy.
- The tracking devices and, in the case of the $\Lambda(1520)$ analysis also the BRICH, were fully operational.

After these cuts, about 1.3 million events remained for the 1994 period and 0.6 million events for the 1995 run around the Z^0 pole. The $\Lambda(1520)$ analysis is based on both years data, the Σ^- analysis only on the 1994 data.

To study the influence of cuts, inefficiencies and resolution as well as particle reinteractions in the detector, a large set of simulated $Z \to q\bar{q}$ events has been used. This simulated sample has been generated using the JETSET 7.3 model [3] with the parton shower option. The model parameters were taken from earlier QCD studies [13]. The initial event simulation was followed by a detailed detector simulation [14]. For the $\Lambda(1520)$ study a specific set of 10000 of these events has also been produced with at least one $\Lambda(1520) \to pK^-$ per event.

2.1 $\Sigma^\pm$ Reconstruction

The charged Σ hyperons decay through the weak interaction according to

$$
\begin{aligned}
\Sigma^+ &\to p\pi^0 \quad (\approx 52\%), \\
&\to n\pi^+ \quad (\approx 48\%), \\
\Sigma^- &\to n\pi^- \quad (\approx 100\%).
\end{aligned}
\tag{1}
$$

The reconstruction of the decay $\Sigma^\pm \to n\pi^\pm$ is based on the large flight length ($c\tau = 4.43$ cm for Σ^- and $c\tau = 2.4$ cm for Σ^+). It allows a determination of the track parameters for the $\Sigma^\pm$, if there are at least three hits in the microvertex detector. The decay

$\Sigma^\pm \to n\pi^\pm$ is then reconstructed by finding the kink between the $\Sigma^\pm$ and the pion which is normally well measured in the other tracking chambers, especially the TPC. Thus, the detection of the neutron is not necessary. The tools needed for the analysis are described in more detail below.

2.1.1   Track reconstruction with the Microvertex Detector

The geometry of the 1994 DELPHI microvertex detector allows the determination of the track parameters of a charged particle in two or three dimensions using information from this detector alone. These tracks, called 'VD tracks' in the following, can arise from:

- Low-momentum charged particles ($p \lesssim 50$ MeV/c) not reaching the TPC due to the bending in the magnetic field.
- Tracks at the borders of the TPC modules not efficiently reconstructed by the standard tracking algorithm.
- Charged particles interacting with the detector material outside the VD.
- Decays such as $X^\pm \to Y^\pm$ + neutral particles (e.g. $\Sigma^\pm \to n\pi^\pm$, $\Xi^- \to \Lambda\pi^-$, $K^\pm/\pi^\pm \to \mu^\pm\nu_\mu$).

To reconstruct these tracks, the microvertex tracking algorithm initially looks for triplets of $R\phi$ hits in the VD (there must be at least one hit in each layer), not associated to tracks reconstructed by the standard tracking algorithm. This allows a determination of the track parameters in the $R\phi$ plane. A second step searches for unassociated z hits in the modules containing the $R\phi$ hits. If there are at least two z hits for a $R\phi$ triplet, the full set of parameters is given for that track. To improve the momentum resolution and to remove products of hadronic interactions in the beampipe, the results from the VD tracking were refitted forcing the track to originate from the primary vertex. The χ^2 probability of this fit had to be greater than 0.1%.

2.1.2   Efficiency correction procedure

To be as independent as possible from the detector simulation, especially from the modelling of the VD, the efficiency for reconstructing a VD track has been deduced directly from the data as follows.

Hadronic interactions in the detector material with at least two outgoing tracks were reconstructed by fitting the candidate tracks to a common vertex. The algorithm allows for an arbitrary number and charge configuration of tracks associated to the vertex[3]. The distribution of the measured positions of these vertices shows the material distribution of the DELPHI detector (Figure 1). If the incoming particle which caused the interaction is charged[4], there is the possibility to reconstruct it as a VD track. To find these particles, the VD tracks were extrapolated to the radius of the interaction vertex and linked as the incoming track to the vertex if the difference in the azimuth angle ϕ between the reconstructed vertex and the VD track was below 1.7°. This cut was chosen to achieve an efficiency and purity for the linking close to unity. These linked VD tracks have not been used as candidates for Σ hyperons to suppress background from hadronic interactions. Finally, hadronic vertices within the polar angle acceptance of the VD were selected and the number of interactions with a link to a VD track was compared to the number of all

---

[3]The charge of the outgoing tracks may not sum up to the charge of the incoming track for hadronic interactions because an atomic nucleus is involved in the reaction.

[4]This is most often the case since the production rate of neutral particles causing hadronic interactions (mainly K_L^0, n and Λ^0) is small compared to the production rate of charged pions, kaons and protons.
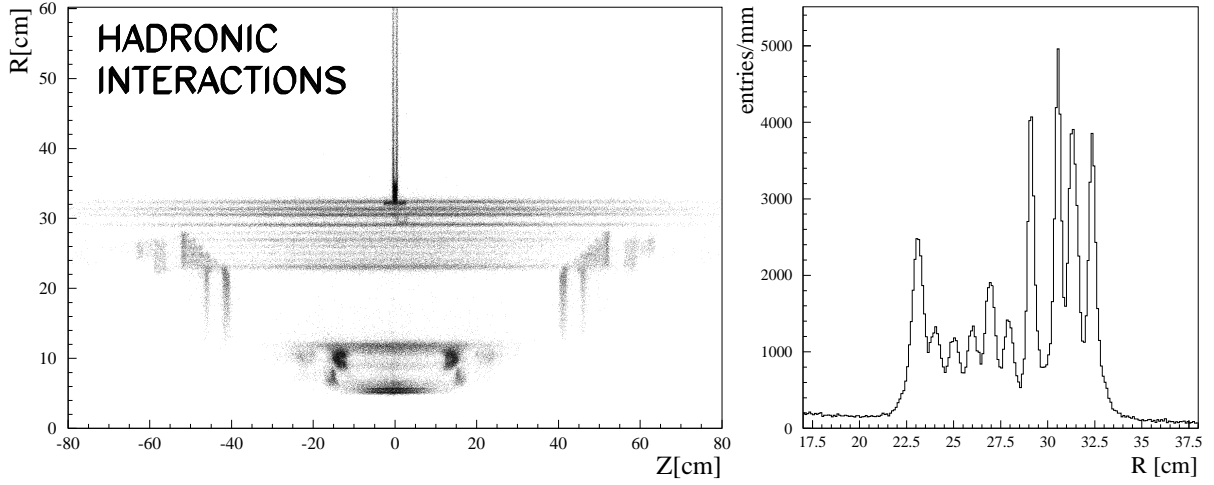
Figure 1: Reconstructed hadronic interactions in the material of the DELPHI detector, used for the determination of the correction factor for the VD track efficiency. Left: Rz view; Right: Radial projection.

selected interactions. The efficiency for reconstructing a VD track is then given through

$$\epsilon_{\text{VD}} = \frac{p_{hv/vd} \cdot N_{hv/vd}}{p_{hv} \cdot N_{hv} \cdot \epsilon_{link} \cdot f_c} \tag{2}$$

where N_{hv} is the number of hadronic vertices, $N_{hv/vd}$ the number of hadronic vertices with a linked VD track, p_{hv} and $p_{hv/vd}$ the purities of these samples[5], ϵ_{link} the efficiency to link the incoming VD track to the vertex and f_c the fraction of charged particles causing hadronic interactions in the detector material. Assuming that the value of f_c is the same in real data and simulation and taking into account the θ dependence by multiplying with the θ distribution of Σ hyperons in simulated events, the following correction factor for the reconstruction efficiency was deduced:

$$r = \frac{\epsilon_{\text{VD}}^{\text{RD}}}{\epsilon_{\text{VD}}^{\text{MC}}} = 0.91 \pm 0.06, \tag{3}$$

where the error is systematic and comes mainly from the uncertainty in the fraction of charged particles causing hadronic interactions, which has been estimated in the following manner. In the region considered for the positions of reconstructed vertices the fraction of charged particles causing the interactions in the simulation was $f_c = 0.84$. As a conservative choice, the error on this fraction was chosen to cover the range up to unity within three standard deviations, thus $f_c = 0.84 \pm 0.053$. It is important to stress that this method does not rely on a precise modelling of the material distribution of the detector because the hadronic vertices were only used as candidate endpoints for the VD tracks.

2.1.3 Reconstruction of the decay $\Sigma^{\pm} \to n\pi^{\pm}$

The candidates for the outgoing pion had to fulfil the following criteria:

- Measured track length > 30 cm.
- $\Delta p/p < 1$.

---

[5]p_{hv} and $p_{hv/vd}$ were estimated directly from the radial distribution of the vertices shown in Figure 1.

- $IP/\sigma_{IP} > 3$ in $R\phi$ and z, where IP denotes the impact parameter with respect to the primary vertex and σ_{IP} its error.
- No associated VD hits in the two innermost layers.
- The track must not originate from a reconstructed hadronic interaction.

The z information of the VD tracks with at least two VD hits was not used in this analysis, because of differences in the association of two z hits between real data and simulation. Thus all VD tracks were treated in exactly the same way.

To find the decay vertex of the $\Sigma^\pm$, the intersections (normally two) in the $R\phi$ plane of the VD track with the previously selected pion candidates were reconstructed. To select the correct intersection point, consistency of this point with the incoming and outgoing track was required which included removing intersections in the hemisphere opposite to the tracks. If both points fulfilled all these cuts, the one with the lower radius was chosen. The z coordinate of this candidate decay vertex was given by the z coordinate of the outgoing pion candidate at this $R\phi$ position. The polar angle θ of the incoming track was calculated using the z coordinates of this vertex and of the primary vertex completing the track parameters of the VD track. The momentum of the (unreconstructed) neutron candidate could be computed allowing the calculation of the invariant mass of the $\Sigma^\pm$-candidate. The combination was rejected if the calculated θ did not lie within the polar angle range covered by the modules of the VD defining the VD track. Both tracks defining the vertex must have the same charge. In order to reject background, the following additional cuts were applied:

- The probability of the particle decaying within the measured flight distance, calculated under the Σ^- hypothesis, had to be lower than 97%. This efficiently removes background from the decays $K/\pi \to \mu\nu_\mu$. Due to their long lifetime ($c\tau(K^\pm) \approx 3.7$ m and $c\tau(\pi^\pm) \approx 7.8$ m) charged kaons and pions decaying inside the sensitive volume of the tracking chambers tend to have very low momenta. Thus, their decay probability as defined above is close to 100%.
- $|\cos\theta^*| < 0.8$, where θ^* denotes the angle between the outgoing track and the VD track, calculated in the rest frame of the particle reconstructed as VD track, where the pion mass was assumed for the measured outgoing track and the neutron mass for the undetected particle.

The resulting mass spectrum of the Σ candidates is shown in Figure 2. A fit with Gaussians for the signal and the reflection from $\Xi^- \to \Lambda\pi^-$ ($c\tau = 4.91$ cm), which has the same signature of a kink[6], and a function of the form

$$F(M) = a_1((M - 1.079)(a_4 - M))^{a_2} \exp(-a_3(M - 0.5(1.079 + a_4))) \tag{4}$$

for the background, where 1.079 is the sum of the masses of the neutron and the pion (in GeV/c^2) and thus the lower kinematical limit, gives a mean mass of 1196.5 ± 0.4 MeV/c^2 and a width $\sigma = 12.3 \pm 0.4$ MeV/c^2, in good agreement with the expectation from simulation of 1197.4 ± 0.3 MeV/c^2 and 12.2 ± 0.6 MeV/c^2, respectively. To subtract the background, two Gaussians with all parameters left free have been used for the signal to take into account the momentum dependence of its width. This results in a measured signal of 4820 ± 109 Σ decays and 870 ± 95 Ξ^- decays (statistical errors only).

---

[6]The decays $\Omega^- \to \Lambda K^-, \Xi^0\pi^-$ also show this signature, but their contribution is negligible due the low Ω^- production rate.
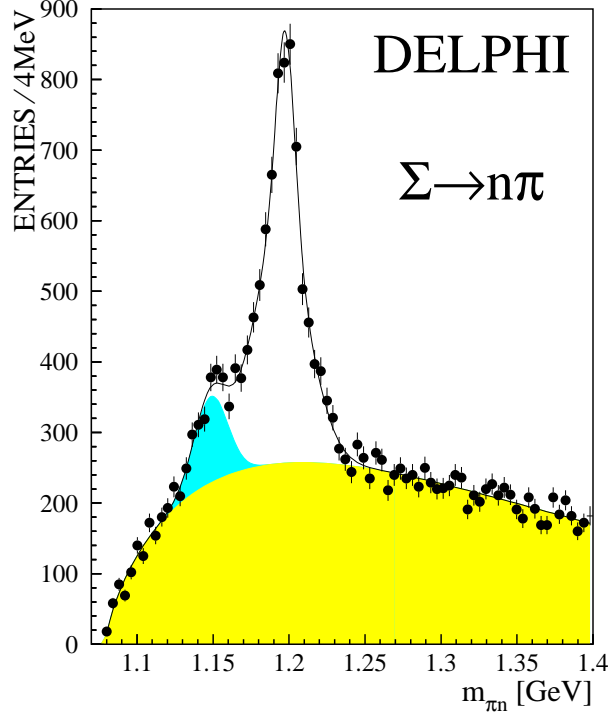
Figure 2: The invariant mass spectrum for the Σ candidates selected as described in the text. Dots are the data. The curve shows the result of a fit with two Gaussians for the signal, one Gaussian for the reflection from the decay $\Xi^- \to \Lambda\pi^-$ (dark shading) and a function of the form (4) for the smoothly varying background (light shading). The χ^2 per degree of freedom of the fit is $\frac{83}{67} = 1.24$.

2.1.4 Measurement of the Σ^- differential production rate

Due to the larger branching ratio into the final state $n\pi$ (see Eq. (1)) and the longer lifetime ($c\tau_{\Sigma^-} \approx 1.8 \cdot c\tau_{\Sigma^+}$), the efficiency to reconstruct the decay $\Sigma \to n\pi$ with the method described above is much higher for the Σ^- than for the Σ^+. To obtain the Σ^- cross-section

$$\sigma_{\Sigma^-} \sim \frac{N}{\epsilon^-} - \frac{1}{a}N_{\Sigma^+}$$

where N denotes the number of signal events, ϵ^- the efficiency for Σ^- reconstruction, $a = \frac{\epsilon^-}{\epsilon^+}$ the ratio of the efficiencies for detecting a Σ^- or Σ^+, and N_{Σ^+} the true number of Σ^+ in the signal, an estimate for the Σ^+ rate to be subtracted has to be made. For this, the ratio of Σ^+ to Σ^- production from the simulation (JETSET 7.4 with default parameters) has been assumed. An error of 20% has been assigned to this ratio. In the x_p bins ($x_p = 2p/\sqrt{s}$) where the deviation of this ratio from unity is greater than 20%, this deviation has been taken as the systematic error.

The differential Σ^- production rate has then been measured in nine x_p bins. For each x_p bin the efficiency has been estimated using the simulated sample with full detector simulation, taking into account the correction factor of equation (3) which was assumed to be independent of x_p. To obtain the number of signal events, the mass spectra have been fitted using a Gaussian function for the signal, a Gaussian function with position and width fixed to the values obtained from the simulation for the reflection $\Xi^- \to \Lambda\pi^-$, and
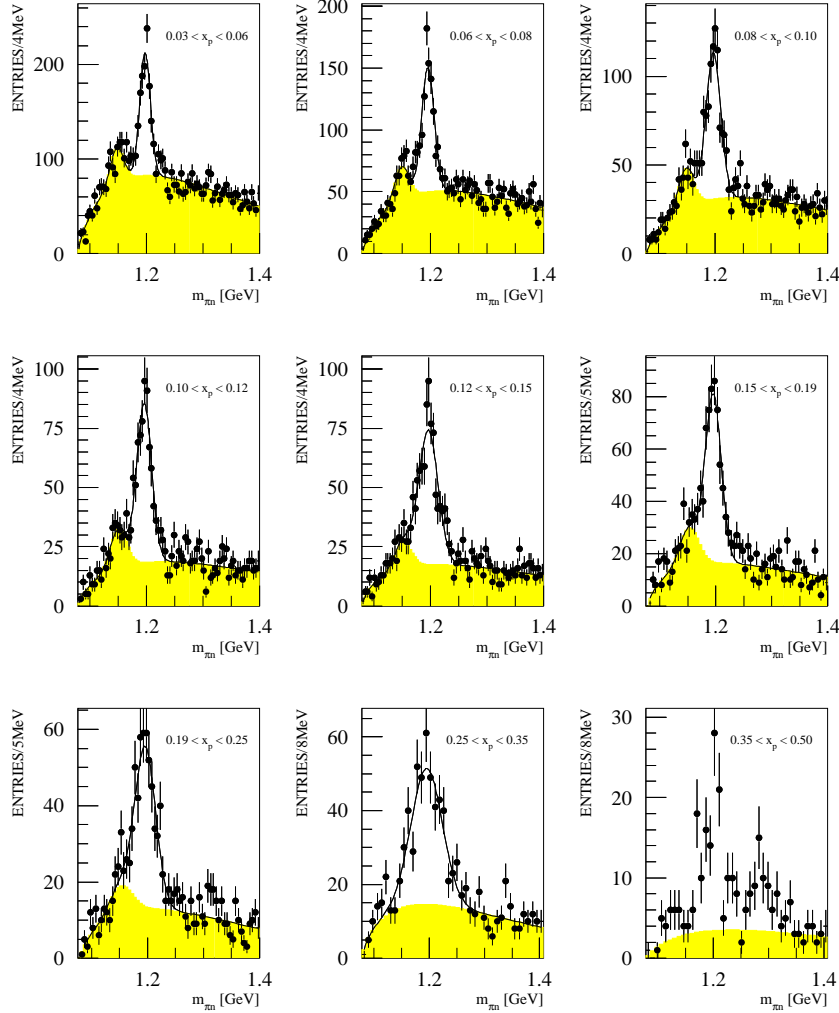
Figure 3: The mass spectra for the different x_p bins. Dots are the data, the solid line shows the result from the fit and the shaded histogram the background used for subtraction.

a function with four free parameters of the form (4) for the smoothly varying background (see Figure 3). The reflection has not been fitted separately for the last two x_p bins due to the large width of the signal. In the last x_p bin the signal has not been fitted, but the background obtained from the simulation (including the contribution from the Ξ-reflection and normalised to data statistics) has been subtracted to get the number of signal events.

2.2 Consistency checks and systematic errors

In addition to the systematic error already mentioned in Section 2.1.2, some more systematic checks have been done to test the consistency between real data and simulation. The quantities used for the selection of the candidates have been compared and good agreement was found. The mass spectrum has been fitted separately for negative and positively charged Σ candidates. One obtains good agreement within the statistical errors (2351 ± 73 and 2298 ± 78 signal events, respectively). Since $a = \frac{\epsilon^-}{\epsilon^+}$ (the values

are given in Table 3) is a function of the decay length of Σ^- and Σ^+, the flight distance distributions for real data and the simulation have been compared for each x_p bin and consistency within the statistical errors has been found.

Since this analysis uses tracks which have been reconstructed using only the microvertex detector of DELPHI, a good internal and external alignment of the VD is essential. It has been checked that the widths obtained for the signal in the different x_p bins show good agreement between real data and simulation within errors. The signal has been fitted separately for both z hemispheres defined through $\cos\theta_{VD-track} \gtrless 0$. Taking into account the θ dependence of the efficiency for reconstructing a VD track (according to (2)), one obtains $N_{\cos\theta<0}/N_{\cos\theta>0} = 1.05 \pm 0.05$ (stat.). Another quantity sensitive to the alignment and effects of the tracking, such as misassociating VD hits to the outgoing pion, is the kink angle between the two tracks. The simulation describes the data well, even for very low values ($\lesssim 5°$) of this angle, where the reconstruction of two distinct tracks and the kink between them is most critical.

To estimate the uncertainty of the number of signal events, the parametrisation of the background and the mass window for the background subtraction have been varied.

The systematic errors due to the efficiency correction and the subtraction of the Σ^+ rate have been added linearly for the different x_p bins and thus treated as fully correlated. Statistical and other systematic errors have been added quadratically from bin to bin. Different systematic errors have been added quadratically. The contributions from the different sources to the total error are listed in Table 1.

error source	absolute unc.	relative unc.
data statistics	0.0016	2.0%
simulation statistics	0.0012	1.5%
efficiency correction (equation (3))	0.0043	5.3%
fit procedure	0.0020	2.5%
Σ^+ rate from simulation	0.0028	3.5%
extrapolation to unobserved x_p region	0.0081	10.0%

Table 1: The uncertainties of the Σ^- production rate.

2.3 $\Lambda(1520)$ Reconstruction

Beyond the general cuts given in Section 2 for this analysis it was required that the track impact parameter to the primary vertex was less than 0.5 mm in the $R\phi$-plane and 1 mm in the z-direction. This requirement strongly reduces contributions of tracks from particle re-interactions inside the detector material. Furthermore there must be at least two tracks inside the angular acceptance $47° < \theta < 133°$ of the BRICH.

The pK$^-$($\bar{\text{p}}$K$^+$) mass-spectra were then constructed for each bin of each individual kinematical variable using identified particles. Particle identification was performed combining dE/dx and BRICH information. According to the quality of particle identification the tagging categories loose, standard and tight tags are distinguished for each particle species as well as for so called "heavy" particles combining protons and kaons. To further improve the quality of particle identification for a track of given momentum and (assumed) particle type it was required that information from the detectors specified in Table (2) was present.

	momentum range in GeV/c						
	0.3 - 0.7	0.7 - 0.9	0.9 - 1.3	1.3 - 2.7	2.7 - 9.0	9.0 -16.0	16.0 - 45.0
π	TPC	LRICH S			GRICH S		
K	TPC	LRICH S			GRICH V + LRICH S	GRICH S	
p	TPC		TPC + LRICH V	LRICH S	GRICH V + LRICH S	GRICH V	GRICH S

Table 2: Momentum ranges for particle identification: TPC denotes identification using the dE/dx measurement of the TPC, LRICH S (V) denotes identification using a signal (veto) of the liquid RICH, and correspondingly GRICH for the gas RICH.

A particle was then taken to be a proton if it was tightly tagged. Kaons were required to be tightly tagged in the momentum ranges $p < 3.5$ GeV/c and $p > 9.5$ GeV/c. In the intermediate momentum range kaons were also identified by a tight heavy particle tag combined with at least a standard kaon tag. To suppress combinatorial background it was required that the kaon momentum was between 28% and 100% of the proton momentum. This condition has been left out for the determination of the $\Lambda(1520)$ spin alignment.

Figure (4a) shows the pK$^-$ mass spectrum of the overall dataset and Figure (4b) for the scaled momentum range $x_p > 0.4$. A clear $\Lambda(1520)$ signal is observed in both mass spectra at about the expected mass. The signal to noise ratio improves for the higher x_p range indicating that a proper measurement can even be performed for high $\Lambda(1520)$ momenta. It should, however, be noted that here the $\Lambda(1520)$ signal became poorly visible if the particle identification requirements were relaxed. It has been checked that there are no prominent reflections from known particle decays in the pK$^-$ mass spectrum.

Particle identification inefficiencies, detector imperfections and the different kinematical cuts imposed for charged particle and event selection, were accounted for by applying the approach first described in [15], developed in [16,17,18,19] and outlined in brief below.

In the present analysis, the mass spectra were described by an anticipated distribution function, $f(M, \vec{a})$, of the invariant mass M. The parameters $\vec{a}$ were determined by a least squares fit of the function to the data. The function $f(M, \vec{a})$ had three components:

$$f(M, \vec{a}) = f^S(M, \vec{a}) + f^B(M, \vec{a}) + f^R(M, \vec{a}), \tag{5}$$

corresponding to the signal (S), background (B), and reflection (R) contributions respectively.

The signal function, $f^S(M, \vec{a})$, described the resonance signal in the corresponding invariant mass distributions. For the pK$^-$ mass distributions it had the form

$$f^S(M, \vec{a}) = a_1 PS(M) \cdot BW(M, a_2, a_3), \tag{6}$$

where the relativistic Breit–Wigner function BW for the $\Lambda(1520)$ is multiplied by the function $PS(M)$ to account for the distortion of the resonance Breit–Wigner shape by phase space effects (see [15] for details).
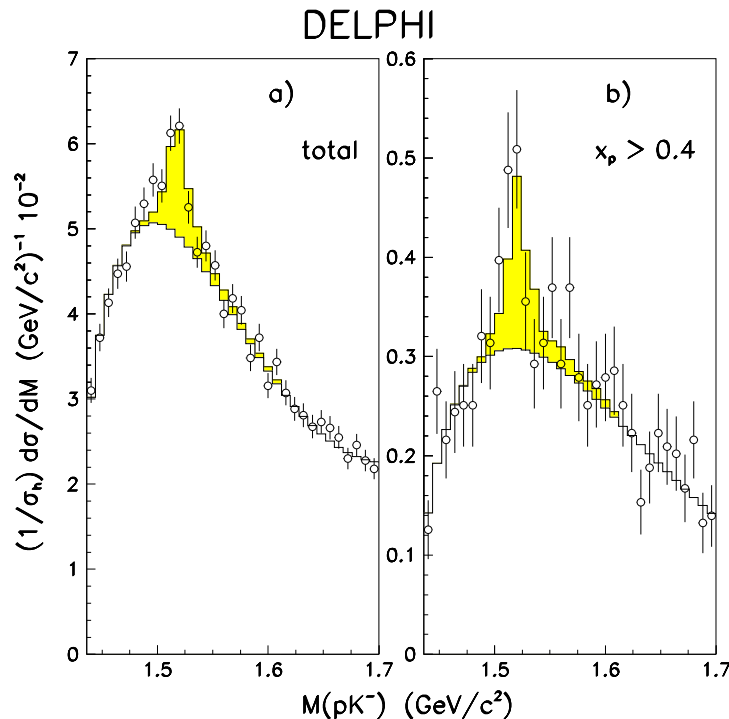
DELPHI

Figure 4: a) Differential pK$^-$ mass spectra for the overall measured energy range. b) pK$^-$ mass spectrum for $x_p > 0.4$. The histograms represent the fit described in the text.

The background term, $f^B(M, \vec{a})$, was taken to be of the form

$$f^B(M, \vec{a}) = BG_{Jetset}(M) \cdot P(M, \vec{a}), \tag{7}$$

where $BG_{Jetset}(M)$ represented the background shape generated by JETSET which describes the gross features of the real background [20] and $P(M, \vec{a}) = 1 + a_4 M + a_5 M^2 + a_6 M^3 + a_7 M^4$ was a polynomial of order four (sometimes a_7 has been fixed to zero) introduced to account for possible deviations of $BG_{Jetset}(M)$ from the real background. All pairs of charged particles which do not come from the resonance considered and reflections in the invariant mass spectra were included in the definition of $BG_{Jetset}(M)$. This parametrisation of the background was different from the analytical form used in a previous DELPHI analysis [15,16,17,18].

The third term, $f^R(M, \vec{a})$, represented the sum of all the reflection functions (RF_i):

$$f^R(M, \vec{a}) = \sum_i a_{i+7} RF_i(M). \tag{8}$$

Reflections arising from particle misidentification and contributing to Equation (8) were considered, for example when resonances in the $\pi^+ K^-$, $K^+ K^-$ and $p\pi^-$ systems (K^{*0}, Φ, Δ^0) distort the pK$^-$ mass spectra. Due to the efficient particle identification of the combined RICH and TPC tags and to the high identification purity provided by the tight cuts, the influence of reflections of this type was found to be much smaller than without particle identification.

The functions $RF_i(M)$ in Equation (8) were determined from events generated according to the JETSET model. The contributions of the reflections to the raw mass spectra defined by the function $\bar{N}_m^R(\vec{a})$ (see Equation (9)) were then obtained by passing these

events through the detector simulation. This also took proper account of the influence of particle misidentification.

In each mass bin, M, the number of entries $\bar{N}_m(\vec{a})$ predicted by the function $f(M, \vec{a})$, representing a sum of contributions from the resonance signal, background and reflections (see [19]), is given by

$$\bar{N}_m^G(\vec{a}) = C_m^G \sum_n S_{mn}^G A_n^G f_n^G(\vec{a}), \tag{9}$$

$$f_n^G(\vec{a}) = \int_{M_n}^{M_{n+1}} f^G(M, \vec{a}) dM, \tag{10}$$

where $G = S$, B or R, and M_n is the lower edge of the n-th histogram bin in the distribution of the variable M. The coefficients A_n characterise the detector acceptance and the losses of particles due to the selection criteria imposed, and the C_m take into account the contamination of the sample by particles from V^0 decays, wrongly associated charged particles, secondary interactions, etc. The smearing matrix S_{mn} represents the experimental resolution. The A_n, C_m and S_{mn} were estimated separately for the resonance signal, background and reflection contributions using the detector simulation program. Due to differences in the detector performance and data processing in different running periods, the simulated events generated for these periods were taken with weights corresponding to the relative number of events in the real data.

The best values for $\vec{a}$ were then determined by a least squares fit of the predictions of Equation (9) to the measured values, N_m, by minimising the function

$$\chi^2 = \sum_m (N_m - \bar{N}_m(\vec{a}))^2 / \sigma_m^2 + \sum_i (a_i - \bar{a}_i)^2 / (\Delta \bar{a}_i)^2, \tag{11}$$

where $\sigma_m^2 = N_m + \sigma^2(\bar{N}_m)$ and $\sigma(\bar{N}_m)$ is the error on $\bar{N}_m$ due to the finite statistics of the simulation used to evaluate A_n, C_m and S_{mn}. The second sum in Equation (11) constrains some of the fitted parameters a_i to the values $\bar{a}_i \pm \Delta \bar{a}_i$ taken from external sources, such as the normalisation of the reflection functions to the particle production rates taken from this and other LEP experiments, and the mass and width taken from the PDG tables [21]. The errors obtained from the fits thus include the corresponding systematic components. As a cross-check the $\Lambda(1520)$ mass was also left free in the fit. This lead to a mass of 1517.5 ± 1.7 MeV/c^2, fully consistent with the PDG value.

In order to determine the full experimental systematic error of the $\Lambda(1520)$ cross-section the following sources of uncertainty were considered. The influence of an imperfect description of stable hadron spectra by the detector simulation was estimated by varying the charged particle selections leading to an associated systematic error of 3%. An error of 9% was assigned due to the imperfect description of $\Lambda(1520)$ production by the fragmentation model. It was estimated by varying kinematical distributions of the $\Lambda(1520)$ like the decay angle and momentum distribution. An uncertainty of 3% on the resonance cross-sections is due to the imperfect description of the particle identification efficiency [22] and the error due to the branching ratios assumed is 2.2% [21]. Uncertainties due to the unknown momentum dependence of the reflections (3%) were assessed by reweighting the shape of the momentum distribution predicted by the model in a range allowed by the fit. Finally the uncertainty in the $\Lambda(1520)$ line-shape, the background parametrisations and the influence of the binning was estimated to be 12% by choosing different parametrisations and by changing the binnings of the mass spectra. Adding the individual contributions in quadrature leads to a final relative experimental error of the $\Lambda(1520)$ cross-section of 16%.

3 Results

3.1 Σ^-

The results for the differential Σ^- production rate and reconstruction efficiencies are listed in Table 3. The differential Σ^- production rate is plotted in Figure 5 together with the predictions of the JETSET 7.4 (default parameters) generator and a previous measurement of the OPAL collaboration [11]. The higher Σ^+ rate compared to the Σ^- rate in JETSET is due to secondary Σ hyperons, mainly from decays of charm particles. The shape of the x_p spectrum is well described in the simulation.

x_p	ϵ^- (%)	$a = \frac{\epsilon^-}{\epsilon^+}$	$\frac{\chi^2}{\text{n.d.f.}}$	N_{Signal}	$\frac{1}{\sigma_{had}}\frac{d\sigma_{\Sigma^-}}{dx_p}$
0.03 - 0.06	2.8 ± 0.1	6.5	1.7	860 ± 52	$0.671 \pm 0.041 \pm 0.064$
0.06 - 0.08	5.6 ± 0.2	4.5	1.2	745 ± 44	$0.422 \pm 0.025 \pm 0.042$
0.08 - 0.10	5.9 ± 0.2	3.4	1.1	725 ± 40	$0.361 \pm 0.020 \pm 0.038$
0.10 - 0.12	6.5 ± 0.3	3.4	1.3	560 ± 34	$0.252 \pm 0.015 \pm 0.032$
0.12 - 0.15	6.2 ± 0.2	3.2	1.1	630 ± 35	$0.195 \pm 0.011 \pm 0.026$
0.15 - 0.19	5.0 ± 0.2	2.7	1.4	470 ± 32	$0.128 \pm 0.009 \pm 0.020$
0.19 - 0.25	4.1 ± 0.2	2.7	1.2	450 ± 29	$0.097 \pm 0.006 \pm 0.016$
0.25 - 0.35	3.7 ± 0.2	2.2	1.2	380 ± 26	$0.051 \pm 0.004 \pm 0.010$
0.35 - 0.50	4.0 ± 0.3	2.2	—	175 ± 17	$0.015 \pm 0.001 \pm 0.005$

Table 3: Efficiencies and differential Σ^- production rate in bins of x_p. The errors given for ϵ^- and N_{Signal} are coming from the simulation and data statistics, respectively.

Integrating the differential production rate in the measured x_p range from 0.03 to 0.5 gives

$$\langle N_{\Sigma^-}/N_{\mathrm{Z}}^{\mathrm{had}}\rangle = 0.065 \pm 0.002 \text{ (stat.)} \pm 0.006 \text{ (syst.)} \quad (\text{JETSET } 7.4\text{: } 0.054).$$

To get the total production rate, the JETSET 7.4 simulated data has been used to extrapolate to the unobserved x_p range. In JETSET 7.4, 18% of the Σ^- hyperons are produced with $x_p < 0.03$ and 2% with $x_p > 0.5$. The production cross-section in this x_p range has been scaled by the ratio of the measured and simulated cross-section in the measured range $0.03 < x_p < 0.5$. This scaled cross-section has then been added and a systematic error of 50% has been assigned to it.

This gives the mean number of Σ^- hyperons produced in multihadronic Z^0 decays

$$\langle N_{\Sigma^-}/N_{\mathrm{Z}}^{\mathrm{had}}\rangle = 0.081 \pm 0.002 \text{ (stat.)} \pm 0.006 \text{ (syst.)} \pm 0.008 \text{ (extr.)},$$

where the last error comes from the extrapolation.

This result is compatible with the corresponding rate in JETSET 7.4 ($\langle N_{\Sigma^-}/N_{\mathrm{Z}}^{\mathrm{had}}\rangle = 0.068$). It is also in good agreement with the measurement from OPAL [11]: $\langle N_{\Sigma^-}/N_{\mathrm{Z}}^{\mathrm{had}}\rangle = 0.083 \pm 0.006 \text{ (stat.)} \pm 0.009 \text{ (syst.)}$.

3.2 $\Lambda(1520)$

The $\Lambda(1520)$ has $J^P = \frac{3}{2}^-$ with isospin 0 and quark content (uds). It decays strongly but with a comparably small decay width of 15.6 ± 1.0 MeV/c^2 as it is a D_{03} state which
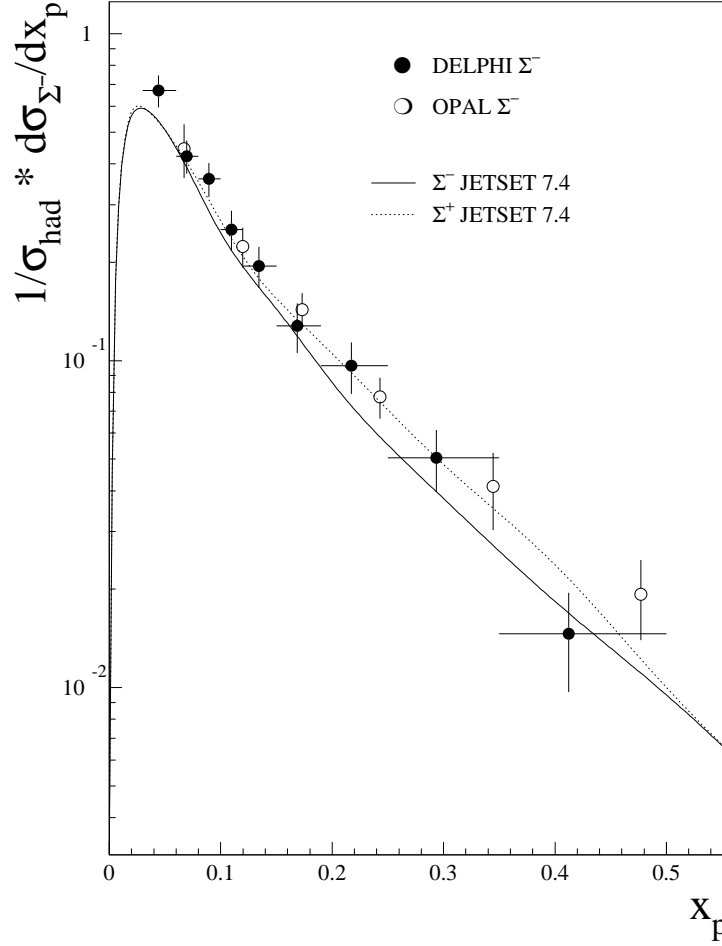
Figure 5: The measured differential Σ^- production rate in comparison with the JETSET model and the OPAL measurement [11]. The data points are plotted at the mean x_p position in the corresponding bin. The statistical and systematic errors have been added quadratically.

predominantly decays into a $J^P = \frac{1}{2}^+$ baryon and one pseudoscalar meson. The $\Lambda(1520)$ branching fraction used in the analysis is taken as half of the branching fraction to nucleon and kaon of 45%:

$$B(\Lambda(1520) \rightarrow pK^-) \simeq 22.5\% \quad .$$

The total $\Lambda(1520)$ rate is measured from a fit to the mass spectrum given in Figure (4a) corresponding to the scaled energy[7] range $0.035 < x_E^{\Lambda(1520)} < 1$:

$$\langle N_{\Lambda(1520)}/N_Z^{had} \rangle = 0.0285 \pm 0.0048 \text{ (fit)} \quad .$$

The fit error includes the statistical error and also accounts for uncertainties in the $\Lambda(1520)$ mass and width and the normalisation of the reflection functions (see Section 2.3). The fitted rate agrees well with the integrated rate from the $\Lambda(1520)$ inclusive x_E spectrum (see below). To estimate the total rate of $\Lambda(1520)$ production this value has to be corrected for the small unmeasured x_E range $x_E^{\Lambda(1520)} < 0.035$. This correction was

---

[7] $x_E^{\Lambda(1520)} = \frac{2E^{\Lambda(1520)}}{\sqrt{s}}$

estimated using a modified JETSET 7.4 model (see below) normalised to the data in the measured momentum range. An additional systematic error of 50% of this correction has been assumed. This yields for the overall $\Lambda(1520)$ production rate

$$\langle N_{\Lambda(1520)}/N_Z^{\mathrm{had}}\rangle = 0.0293 \pm 0.0049 \text{ (fit)} \pm 0.0047 \text{ (syst.)} \pm 0.0003 \text{ (extr.)}$$

including the systematic errors considered in Section 2.3. This result is slightly higher than, though fully consistent with, the OPAL result [9].

In order to exclude that the observed $\Lambda(1520)$'s originate predominantly from heavy (b,c) particle decays the $\Lambda(1520)$ production has been determined individually for samples strongly enriched in b-quarks and light quarks respectively [20]. This enrichment relies on increased particle impact parameters due to the high lifetime of B hadrons [23]. No significant change in $\Lambda(1520)$ production has been found in either sample which leads to the conclusion that the dominant part of $\Lambda(1520)$ production originates from fragmentation.

The observed $\Lambda(1520)$ rate is comparable to that of the $\Sigma^{*\pm}(1385)$ [9,10,24] which has the same strangeness and total spin. It can be concluded that the orbital excitation ($L = 1$) of the $\Lambda(1520)$ does not lead to a suppression of particle production. The comparably large observed $\Lambda(1520)$ rate suggests that also other orbitally excited baryonic states are produced in fragmentation. In consequence, due to the vast amount of orbitally excited states, a large part of the observed stable baryons may descend from these excited states. This agrees with the expectations of the phenomenological models [5,6]. Thus for baryons the situation is likely to be similar to the mesonic case. It is highly desirable to verify the production of other orbitally excited baryonic states, however, this is experimentally demanding due to the large width and complicated decay modes of these states.
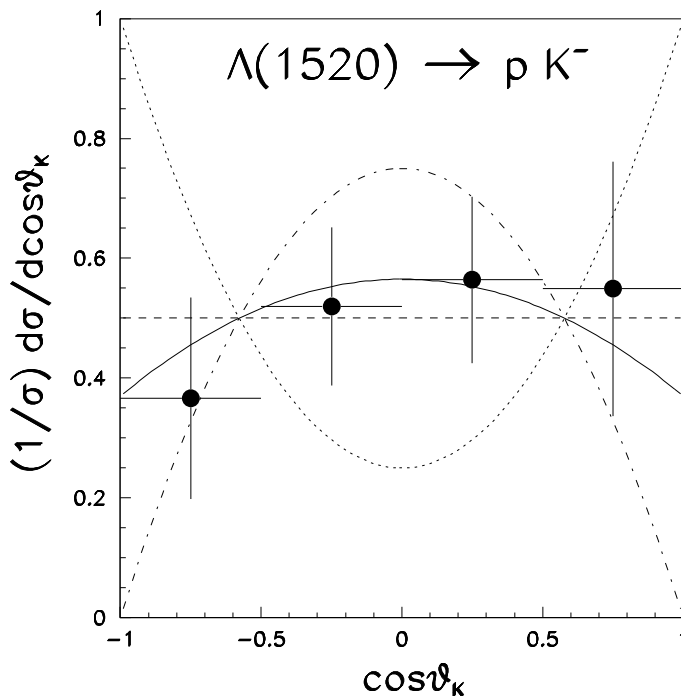

Figure 6: Differential $\Lambda(1520)$ distribution as function of $\cos\vartheta_K$ for $x_p > 0.07$. The full line represents the result of a fit of the angular distribution, the dashed line represents the expectation for unaligned $\Lambda(1520)$'s and the dotted (dash-dotted) line represents the expectation for $\rho_{\frac{1}{2}\frac{1}{2}} + \rho_{-\frac{1}{2}-\frac{1}{2}} = 1$ (0).

In order to determine a possible spin alignment of the $\Lambda(1520)$'s the distribution of the cosine of the kaon angle, $\cos\vartheta_K$, in the $\Lambda(1520)$ rest system with respect to the $\Lambda(1520)$ direction is plotted in Figure (6) for $x_p > 0.07$. This distribution has been fitted with the expected form of the angular distribution:

$$W(\cos\vartheta_{\mathrm{K}}) = \rho\frac{1 + 3\cos^2\vartheta_{\mathrm{K}}}{4} + (1 - \rho)\frac{3 - 3\cos^2\vartheta_{\mathrm{K}}}{4} \tag{12}$$

with $\rho = \rho_{\frac{1}{2}\frac{1}{2}} + \rho_{-\frac{1}{2}-\frac{1}{2}}$, ρ_{ii} denoting the spin-density matrix element. The fit yields $\rho = 0.4 \pm 0.2$, thus no significant $\Lambda(1520)$ spin alignment is observed. The specified error includes the statistical error and the error due to the uncertainty in the background shape.

Furthermore, the approximate symmetry of this distribution with respect to $\cos\vartheta_K = 0$ presents evidence for the validity of this analysis as possible errors in particle identification and corrections would, in general, lead to a distorted $\cos\vartheta_K$ distribution.
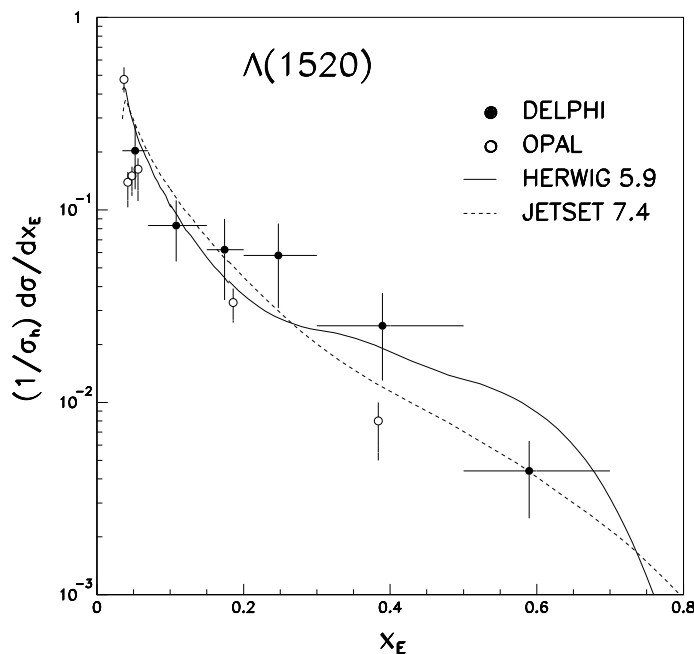

Figure 7: Inclusive $\Lambda(1520)$ distribution as function of x_E. Horizontal error bars indicate the bin width, vertical error bars are the fit errors described in the text.

The measured scaled energy $x_E^{\Lambda(1520)}$ distribution is given in Table (4) and shown in Figure (7) compared to the OPAL result [9]. At low x_E both measurements agree within error. For $x_E > 0.3$ this measurement yields a rate about three times higher. Note that in this energy range a clear $\Lambda(1520)$ signal is observed (see Figure (4b)). The measurements are compared to predictions of modified HERWIG 5.9 and JETSET 7.4 models. $\Lambda(1520)$ production has been implemented in these models either by replacing the $\Sigma^{*0}(1385)$ by the $\Lambda(1520)$ in the case of JETSET 7.4 or by adding only the $\Lambda(1520)$ to the particle list in case of HERWIG 5.9. The predicted rates should not be expected to be well reproduced by the models and the model predictions have been renormalised to the observed $\Lambda(1520)$ rate. The general shape of the fragmentation function is reproduced well by both models.

x_E-range	$\langle x_E \rangle$	$1/N_{evt.} \cdot dN^{\Lambda(1520)}/dx_E$	χ^2/N_{df}
$0.035 - 0.07$	0.052	$0.203 \pm 0.068 \pm 0.032$	28 / 27
$0.07 \ - 0.15$	0.108	$0.083 \pm 0.026 \pm 0.013$	32 / 27
$0.15 \ - 0.20$	0.174	$0.062 \pm 0.026 \pm 0.010$	18 / 27
$0.20 \ - 0.30$	0.247	$0.058 \pm 0.025 \pm 0.009$	25 / 27
$0.30 \ - 0.50$	0.390	$0.025 \pm 0.011 \pm 0.004$	48 / 27
$0.50 \ - 0.70$	0.590	$0.0044 \pm 0.0018 \pm 0.0007$	32 / 27

Table 4: Differential $\Lambda(1520)$ distribution as function of the scaled $\Lambda(1520)$ energy $x_E^{\Lambda(1520)}$. The first error is the fit error, the second error the systematic error (see Section 2.3). The χ^2/N_{df} specifies the quality of the fits.

In order to demonstrate the importance of $\Lambda(1520)$ production in Figure (8) the ratio of $\Lambda(1520)$ to Λ production is shown as function of the scaled momentum x_p. For this comparison the measurement of [24] is taken as it covers a similar range in scaled momentum like this $\Lambda(1520)$ measurement. It is seen that at small x_p, $\Lambda(1520)$ production is about a factor 20 less than Λ production. At large x_p, however, this reduces to a factor $\sim$2.5. Such a behaviour would be expected from general fragmentation dynamics due to the higher mass of the $\Lambda(1520)$. An increase of this ratio is also expected if many Λ's stem from resonance decays. Finally it is interesting to note that the ratio of $\Lambda(1520)$ to proton production is identical, within error, at low energies [8] and in hadronic Z decays (as calculated from this result and [22]).

3.3 Discussion on baryon multiplicities

The measured Σ^- and $\Lambda(1520)$ production rates may now be more generally compared to the LEP average values for all baryons [25]. In Figure (9a) the sum of the production rates of all states of an isomultiplet from the well known baryon octet and decuplet and for the orbitally excited isoscalar $\Lambda(1520)$ are shown as a function of the corresponding particle mass squared, M^2. In the case that not all states of an isomultiplet are measured at LEP, equal production rates for these states are assumed. Therefore the vertical axis of the Figure (9a) is denoted by $(2I + 1) \langle n \rangle$, where $\langle n \rangle$ is the mean number of a given particle per hadronic Z^0 decay. It is seen that the mass dependence of the production rates is almost identical for the following sets of baryons:

1. N, Δ with strangeness S=0;
2. Σ, Σ^*, Λ and $\Lambda(1520)$ with S=1 and
3. Ξ, Ξ^* with S=2.

Finally the Ω^- rate is well predicted if the same mass dependence with an additional suppression for the higher strangeness (S=3) is assumed, as taken from the difference of the first and second or second and third set, respectively. All data points from these three sets and the Ω^- are well fitted ($\chi^2/ndf = 5.9/6$) by the ansatz (see dotted lines in Figure (9a))

$$\gamma^{-S} (2I + 1) \langle n \rangle = A \exp(-b M^2). \tag{13}$$

The values of the fitted parameters are: $A = 20.1 \pm 1.5$, $\gamma = 0.482 \pm 0.022$ and $b = 2.61 \pm 0.08$ $(\text{GeV}/c^2)^{-2}$. As decays of high mass particles feed down to lower mass states,
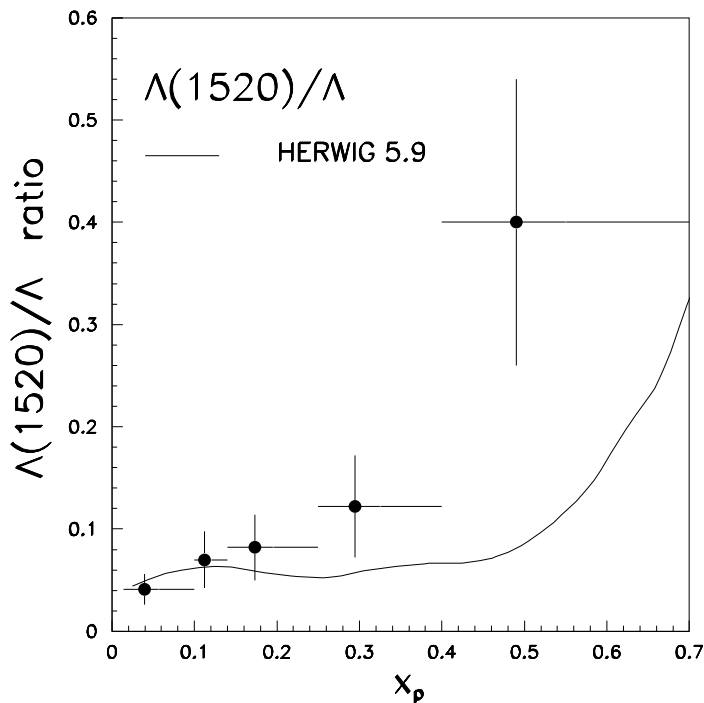
Figure 8: Ratio of the differential x_p distributions of $\Lambda(1520)$'s and Λ's. Λ data are taken from [24].

it is to be expected that especially the slope parameter b for primary produced baryons differs from the fitted value. If the production rates are weighted by γ^{-S} a universal mass dependence is observed for all baryons (see Figure (9b)).

A similarly simple behaviour was found for scalar, vector and tensor mesons [26]. Note that for mesons the production rates per spin and isospin projection were used. This is implicit in the figures shown in [26], as the experimental rates for mesons are customarily specified for each isospin state individually. The mass dependence for mesons, contrary to the baryonic case is exponential in mass, M, thus for mesons

$$\gamma^{-k} \frac{1}{2J+1} \langle n \rangle = A \exp(-b\,M) \quad , \tag{14}$$

where k is the number of s and $\bar{s}$ quarks in the meson. For baryons and mesons an almost identical value of $\gamma \approx 0.5$ was found. A stronger fall-off with the mass for baryons, compared to mesons, is to be expected as baryons are produced in pairs.

4   Conclusions

The differential cross-section of the Σ^- hyperon has been measured in multihadronic Z decays by reconstructing the kink between the Σ^- and the outgoing pion in the decay $\Sigma^- \to n\pi^-$. The measured production rate is

$$\langle N_{\Sigma^-}/N_Z^{\mathrm{had}} \rangle = 0.081 \pm 0.002 \,(\text{stat.}) \pm 0.006 \,(\text{syst.}) \pm 0.008 \,(\text{extr.}) \quad .$$

This result is about 20% above the prediction of the JETSET 7.4 model, but nevertheless compatible. The shape of the differential cross-section is well described in this model.
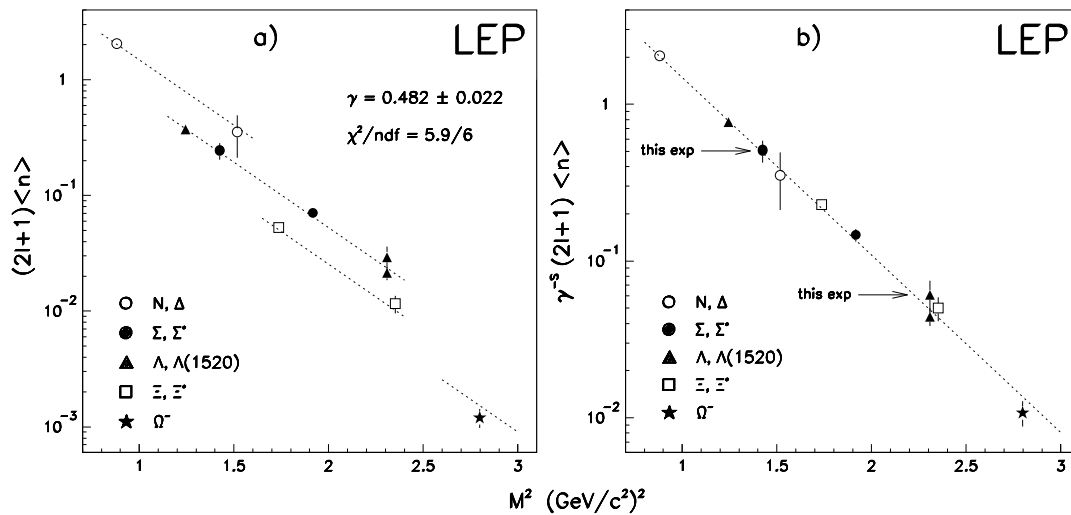
Figure 9:   a) Sum of the baryon production rates of all states of an isomultiplet as a function of the squared baryon mass. Data were taken from [25]. b) Sum of the baryon production rates of all states of an isomultiplet weighted by γ^{-S} as a function of the squared baryon mass.

The differential cross-section of the orbitally excited $\Lambda(1520)$ baryon has been measured relying strongly on the particle identification capabilities of the DELPHI detector. The $\Lambda(1520)$ is the only measured orbitally excited baryon produced in fragmentation at LEP. Its production rate is found to be

$$\langle N_{\Lambda(1520)}/N_Z^{\mathrm{had}} \rangle = 0.0293 \pm 0.0049(\mathrm{fit}) \pm 0.0047(\mathrm{syst.}) \pm 0.0003(\mathrm{extr.}) \quad .$$

This rate is similar to that of the $\Sigma^{*\pm}(1385)$ and suggests that also other orbitally excited baryonic states are produced in fragmentation. The shape of the $\Lambda(1520)$ fragmentation function is well described by the JETSET 7.4 and HERWIG 5.9 fragmentation model if $\Lambda(1520)$ production is introduced.

It has also been shown that the production rates of all baryonic states measured so far at LEP can be parametrised by a phenomenological law.

Acknowledgements

References

[1] For a recent review see: I.G. Knowles and G.D. Lafferty, J. Phys. **G23** (1997) 731.

[2] G. Marchesini et al., Comp. Phys. Comm. **67** (1992) 451.

[3] T. Sjöstrand, Comp. Phys. Comm. **82** (1994) 74.

[4] F. Becattini, Z. Phys. **C69** (1996) 485.

[5] P.V. Chliapnikov and V.A. Uvarov, Phys. Lett. **B345** (1995) 313.

[6] Yi-Jin Pei, Z. Phys. **C72** (1996) 39.

[7] P.V. Chliapnikov, Phys. Lett. **B462** (1999) 341;
P.V. Chliapnikov, Phys. Lett **B470** (1999) 263.

[8] ARGUS Collab., H. Albrecht et al., Phys. Rep. **276** (1996) 223.

[9] OPAL Collab., G. Alexander et al., Z. Phys. **C73** (1997) 569.

[10] DELPHI Collab., P. Abreu et al., Z. Phys. **C67** (1995) 543.

[11] OPAL Collab., G. Alexander et al., Z. Phys. **C73** (1997) 587.

[12] DELPHI Collab., P. Aarnio et al., Nucl. Instr. and Meth. **A303** (1991) 233;
DELPHI Collab., P. Aarnio et al., Nucl. Instr. and Meth. **A378** (1996) 57.

[13] DELPHI Collab., P. Abreu et al., Z. Phys. **C73** (1996) 11.

[14] DELSIM User's Guide, DELPHI Note 89-15 PROG 130;
DELSIM Reference Manual, DELPHI Note 89-68 PROG 143.

[15] DELPHI Collab., P. Abreu et al., Z. Phys. **C65** (1995) 587.

[16] DELPHI Collab., P. Abreu et al., Z. Phys. **C73** (1996) 61.

[17] DELPHI Collab., P. Abreu et al., Phys. Lett. **B361** (1995) 207.

[18] DELPHI Collab., P. Abreu et al., Phys. Lett. **B406** (1997) 271.

[19] DELPHI Collab., P. Abreu et al., Phys. Lett. **B449** (1999) 364.

[20] F. Seemann, Diplomarbeit, Bergische-Univ. Wuppertal, WUD 98-28.

[21] Particle Data Group, Eur. Phys. J. **C3** (1998) 1.

[22] DELPHI Collab., P. Abreu et al., Eur. Phys. J. **C5** (1998) 585.

[23] G. Borisov and C. Mariotti, Nucl. Instr. and Meth. **A372** (1996) 181.

[24] ALEPH Collab., R. Barate et al., Phys. Rep. **294** (1998) 1.

[25] ALEPH Collab., R. Barate et al., Eur. Phys. J. **C5** (1998) 205;
DELPHI Collab., W. Adam et al., Z. Phys. **C70** (1996) 371;
L3 Collab., M. Acciari et al., Phys. Lett. **B407** (1997) 389;
OPAL Collab., R. Akers et al., Z. Phys. **C63** (1994) 181;
OPAL Collab., G. Alexander et al., Phys. Lett. **B358** (1995) 162;
see furthermore References [9,10,11,17,22,24].

[26] V. Uvarov, Proceed. of the XVth Particles And Nuclei International Conference (Uppsala, 1999), Eds. G. Fäldt et al., Nuclear Physics A (in press).